RSC Advances

PAPER

View Article Online
View Journal | View Issue

Cite this: RSC Adv., 2015, 5, 44121

A comparative study of high pressure behaviors of pyrochlore-type and thortveitite-type $In_2Ge_2O_7$

Hui Li,[a] Yan Li,[ab] Nana Li,[c] Yongsheng Zhao,[a] Hongyu Zhu,[a] Pinwen Zhu*[a] and Xin Wang*[a]

Received 16th March 2015
Accepted 11th May 2015

DOI: 10.1039/c5ra04587h

www.rsc.org/advances

Polycrystalline $In_2Ge_2O_7$ with a monoclinic structure (thortveitite-type, T-type) and a cubic structure (pyrochlore-type, P-type) have been synthesized by using different methods. The structural stabilities and electrical transport properties of these two polymorphs under high pressure have been investigated by angle-dispersive X-ray diffraction (ADXRD) and alternate current (AC) impedance spectra. An irreversible structural phase transition from monoclinic ($C2/m$) to another monoclinic ($P2_1/c$) phase has been found in the T-type $In_2Ge_2O_7$ above 6.6 GPa. Furthermore, the pressure dependent electrical resistance of the T-type $In_2Ge_2O_7$ shows a dramatic change at 5.3 GPa, where it can be attributed to the observed pressure-induced structural phase transition. On the contrary, the P-type $In_2Ge_2O_7$ with the cubic ($Fd\bar{3}m$) structure at high pressure is much more stable up to 26.5 GPa.

Introduction

In the past few decades, there has been increasing interest in pyrochlore oxide materials (general formula $A_2B_2O_7$) for studies both in basic science[1–6] and engineering.[7–11] Since different A and B ions can reside on two distinct interpenetrating lattices of corner-sharing tetrahedra, a diverse range of constituent ions can be chosen to obtain the desired properties. Pyrochlore oxides have been reported to show various electrical transport properties, such as superconductivity in $Cd_2Re_2O_7$,[12] an unconventional anomalous Hall effect in $Nd_2Mo_2O_7$ and $Pr_2Ir_2O_7$,[13] and metal-insulator transition (MIT) in $Cd_2Os_2O_7$,[14,15] $Tl_2Ru_2O_7$,[16] and $Hg_2Ru_2O_7$.[17] In addition, very rich exotic magnetic ground states have been discovered, such as spin glass behavior in $Y_2Mo_2O_7$,[18] spin ice in $Ho_2Ti_2O_7$, $Dy_2Ti_2O_7$, and $Ho_2Sn_2O_7$,[19,20] *etc.* Moreover, some pyrochlores have been intensively investigated for widespread applications in the use for fluorescence centers, catalysts,[21,22] or as cathode and electrolyte materials in solid oxide fuel cells.[23–26] Besides, over the past few years, the studies of thin-film pyrochlores have attracted a lot of attentions.[27–29]

Among these pyrochlore oxides, rare-earth based pyrogermanates ($Ln_2Ge_2O_7$) have attracted considerable attentions due to the potential applications in deep-ultraviolet photodetection, ion exchanges, humidity sensors, and high energy laser systems.[30] From structural point of view, rare-earth pyrogermanates possess a variety of crystal structures at ambient condition, such as triclinic phase for Ln = La, Pr, Nd–Gd; tetragonal phase for Ln = Gd–Lu; monoclinic phase for $Sc_2Ge_2O_7$. Moreover, depending on the synthesis method, different structural modifications of $Ln_2Ge_2O_7$ can be obtained. By conventional solid state synthesis, $In_2Ge_2O_7$ has the monoclinic structure (T-type). However, the cubic phase (P-type) of $In_2Ge_2O_7$ can be synthesized by the high-pressure and high-temperature (HPHT) method.[31] By the same method, other examples showed that the P-type silicate pyrochlore $Sc_2Si_2O_7$ and $In_2Si_2O_7$ could be obtained at 1273 K under 12 GPa[32] and also the P-type $Mn_2V_2O_7$ could be prepared at 1373 K under 7 GPa.[33] In these P-type pyrochlores, the structural stabilities at high pressures have been widely studied. For instance, the transformation to the distorted defect-fluorite structure was observed in $Sm_2Zr_2O_7$ above 18 GPa[34] and in $Gd_2Zr_2O_7$ above 15 GPa.[35] Pressure-induced amorphization was found in $Gd_2Ti_2O_7$ above 32 GPa.[36] Also, by applying high pressure, some novel physical properties could be discovered in these materials. For example, pressure-induced transition from a correlated insulator to a Fermi liquid state was observed in geometrically frustrated $Hg_2Ru_2O_7$.[17] At ambient pressure $Tb_2Ti_2O_7$ remained in a spin liquid state down to 70 mK, but under high pressure, the spin ordering appeared around 2.1 K.[3] Therefore, the understanding of underlying relationship between the exotic behaviors and the structural aspects at high pressures is of importance to these pyrochlore materials. As an important ternary oxide with excellent photoluminescence properties, the luminescence appeared as characterizing charge transfer transitions in indium groups (InO_6 octahedra) is closely related to the crystal structure of $In_2Ge_2O_7$.[37,38] So the work to study the structural properties of $In_2Ge_2O_7$ with different phases under

[a]State Key Laboratory of Superhard Materials, Jilin University, Changchun 130012, China. E-mail: xin_wang@jlu.edu.cn; zhupw@jlu.edu.cn

[b]College of Physics, Jilin University, Changchun 130012, China

[c]Center for High Pressure Science and Technology Advanced Research, Shanghai 201203, China

high pressure will be beneficial to explore the possibility of using the material for the application in optoelectronic devices.

In the present study, we have studied the structural stability of the two polymorphs of $In_2Ge_2O_7$ and analyzed their detailed structural evolutions at high pressures. An irreversible pressure-induced structural phase transition is found in the T-type $In_2Ge_2O_7$. Meanwhile, we have also carried out the high-pressure AC impedance spectra measurements to detect the variation of electrical transport properties during the structural phase transition.

Experimental

Sample preparation

The T-type $In_2Ge_2O_7$ was synthesized by standard solid state reaction method. Stoichiometric quantities of In_2O_3 (99.99%) and GeO_2 (99.9%) were mixed and ground thoroughly in an agate mortar. The obtained powder was pressed into small pellets and then calcined at 1473 K in air for 5 h. The P-type $In_2Ge_2O_7$ was synthesized by the HPHT method. The as-prepared powders were assembled and loaded into a cubic anvil HPHT apparatus (SPD-6×600) at a temperature of 1573 K and a pressure of 5.2 GPa with a holding time of 15 min.

X-ray diffractometry

The phase purity was detected by powder X-ray diffraction measurements using Rigaku Rotaflex X-ray diffractometer with Cu-Kα radiation at ambient pressure. A diamond anvil cell (DAC) was utilized to generate high pressure with the T301 stainless steel as the gasket, which was preindented to a 50 μm thickness. The high-pressure angle-dispersive XRD spectra were collected at the beamline 4W2 of Beijing Synchrotron Radiation Facility for the T-type $In_2Ge_2O_7$ with a monochromic wavelength of 0.6199 Å and at the beamline X17C of the National Synchrotron Light Source at Brookhaven for the P-type $In_2Ge_2O_7$ with a wavelength of 0.4073 Å. In the above experiments, one piece of the respective samples and a small piece of ruby as pressure calibrant[39] were loaded into DAC with a 16 : 3 : 1 methanol/ethanol/water mixture as pressure-transmitting medium. Distance between sample and detector, and parameters of detector were calibrated using a CeO_2 standard. All the diffraction data were collected using a MAR CCD detector and the diffraction profiles were obtained *via* the radial integration of the two-dimensional diffraction rings using FIT2D software. Rietveld analyses were performed with the software GSAS.[40]

Alternate current (AC) impedance spectra at high pressures

van der Pauw electrodes were integrated on one facet of DAC with 300 μm in diameter for the electric properties measurement under high pressure. The sample chamber is about 100 μm in diameter and 70 μm in thickness. The measurements of AC impedance spectra in the frequency range of 1 Hz to 10 MHz at pressures up to 13.2 GPa were carried out by using Solartron 1260 impedance analyzer equipped with a Solartron 1296 dielectric interface. The applied AC voltage was 0.1 V.

Results and discussion

Crystal structures at ambient condition

The observed and calculated XRD patterns together with their differences of two types of $In_2Ge_2O_7$ are shown in Fig. 1. The diffraction peaks in Fig. 1a match well with the monoclinic structure $In_2Ge_2O_7$ (T-type, S.G. $C2/m$, no.12) and the obtained cell parameters are: a = 6.6598(3) Å, b = 8.7842(5) Å, c = 4.9244(3) Å, β = 102.588(5)°, V = 281.17(1) Å^3 with Z = 2. In this kind of crystal structure, In^{3+} cations are distributed in the center of distorted InO_6 octahedra that are joined by edge sharing forming a hexagonal arrangement on the *ab* plane. The InO_6 octahedra layers are held together by sheets of isolated Ge_2O_7 diorthogroups constituted by double tetrahedra sharing a common vertex, as shown in Fig. 2a.

The refined XRD pattern of the P-type $In_2Ge_2O_7$ is presented in Fig. 1b. It belongs to cubic system (S.G. $Fd\bar{3}m$, no.227) with the lattice parameters of a = 9.7121(3) Å and Z = 8. In this cubic phase, it can be formulated as $In_2Ge_2O_6O'$ and the Ge ion sites at 16c, In at 16d, O at 48f and O′ at 8b site. The In site (16d) coordination polyhedron is a distorted cube that generally contains larger cations, and the Ge site (16c) is a distorted octahedron. It is worth noting that there is only one adjustable positional parameter x for the O atom at 48f site. The schematic illustration of the P-type $In_2Ge_2O_7$ is shown in Fig. 2b.

Structural phase transition of the T-type $In_2Ge_2O_7$ under high pressure

The *in situ* XRD patterns of the T-type $In_2Ge_2O_7$ at various pressures up to 35.4 GPa have been collected and a few representative patterns are shown in Fig. 3. At the beginning, all the diffraction peaks shift toward higher 2θ angles with increasing pressures. When the applied pressure is above 6.6 GPa, it can be clearly seen that some new peaks are emerging from the original phase, which are indicated by the closed circles as shown in Fig. 3. The new high-pressure phase and the thortveitite

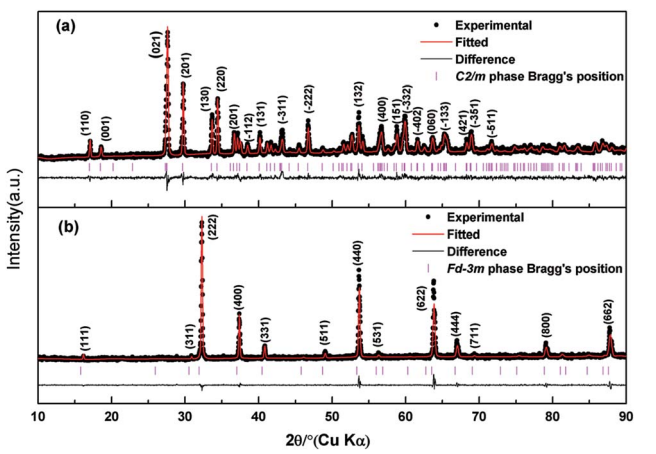

Fig. 1 Observed, calculated and difference X-ray powder patterns of $In_2Ge_2O_7$ at ambient pressure: (a) Rietveld refinement for the T-type $In_2Ge_2O_7$ in monoclinic ($C2/m$) phase and (b) Rietveld refinement for the P-type $In_2Ge_2O_7$ in cubic ($Fd\bar{3}m$) phase.

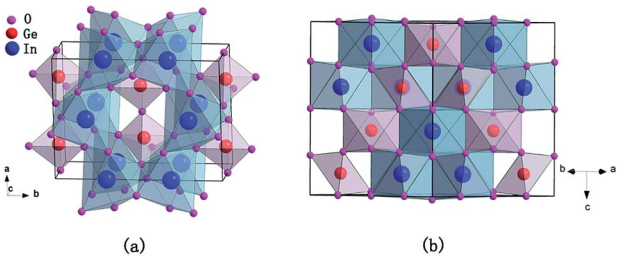

Fig. 2 A Schematic representation of the crystal structures of (a) the T-type and (b) the P-type $In_2Ge_2O_7$.

structure coexist over a wide pressure range between 6.6 and 17.4 GPa. The strong hysteresis comes across this transition, and it can be attributed to the inherent sluggish nature of the transition and the kinetic effects of the first-order transition. Above 17.4 GPa, the new high-pressure phase of the T-type $In_2Ge_2O_7$ becomes dominant up to the highest pressure. The broad peaks and high background in the patterns indicate that the high pressure phase is probably highly disordered. As the sample is recovered from 35.4 GPa, it show that the pressure-induced structure transition is irreversible. Direct method of structure determination is adopted and the new high pressure phase can be explained using another monoclinic unit cell based on $P2_1/c$ phase (S.G. 14, $Z = 1$), which is verified by Rietveld refinements as shown in Fig. 4. This type of high-pressure phase has also been observed in $Gd_2Zr_2O_7$.[35] The lattice parameters and refined atomic coordinates at 17.4 GPa are listed in Table 1, in which it also contains the structural data of the T-type and P-type $In_2Ge_2O_7$ at ambient pressure for comparison.

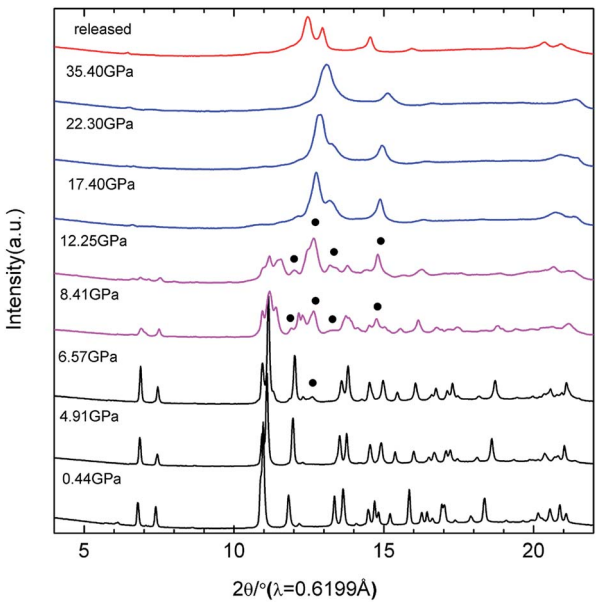

Fig. 3 Selected XRD patterns of the T-type $In_2Ge_2O_7$ at different pressures. A high-pressure phase appeared at 6.6 GPa and the phase transition is completed above 17.4 GPa. The quenched sample remains the high-pressure phase. New emerging peaks are marked by the closed circles.

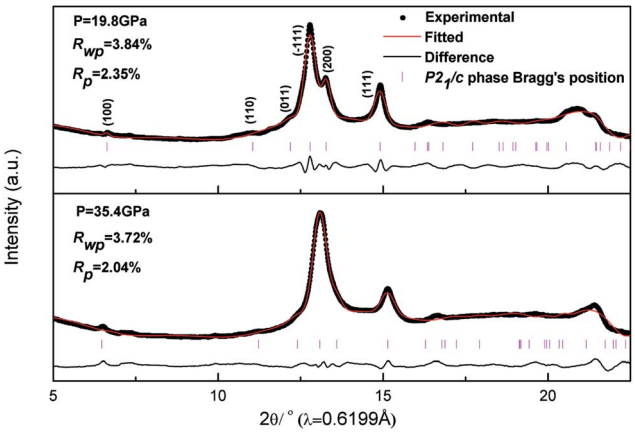

Fig. 4 Observed and calculated diffraction patterns of the T-type $In_2Ge_2O_7$ at 19.8 and 35.4 GPa, respectively. The difference curve and the tick marked for the calculated reflection positions are plotted at the bottom of the figure.

All the XRD data have been analyzed by Rietveld refinements and pressure dependences of the lattice parameters of the T-type $In_2Ge_2O_7$ are shown in Fig. 5. At the pressure point of structural phase transition, it can be seen that the lattice constants have a large decrease of 13.2%, 52.1% and 7.2% for *a*-, *b*- and *c*-axis, respectively. The collapse along *b*-axis is much larger than the collapse along *a*- and *c*-axis. Consequently, the phase transition is accomplished by the reconstruction of the anion and cation sublattices, and the schematic structural transformation (in *ab* and *ac* plane) is shown in Fig. 6. The transformation process of the T-type $In_2Ge_2O_7$ from $C2/m$ to $P2_1/c$ phase is illustrated from left side to right side in the figure. In the process of phase transition, the coordination number is also changed from 6 to 7 for In^{3+} cations and from 4 to 7 for Ge^{4+} cations. Ge^{4+} cations are more likely to move to the empty space in the arrow direction in *ab* plane as shown in the upper part of Fig. 6 and then drive In1 and In4 ions much closer to each other upon compression, which indicates that the compressibility along In1–In4 direction is larger than other directions. In addition, in the lower part of the figure, we can see that the layered structure becomes much denser after the phase transition in *ac* plane. Also, it can explain that the change along *b*-axis is much larger than the changes along *a*- and *c*-axis.

Fig. 7 shows the pressure-volume data for the T-type $In_2Ge_2O_7$. A large volume drop by approximate 23.9% is observed at the phase transition implying that the transformation to the high pressure phase is the first order. Since $In_2Ge_2O_7$ is typical of ionic solid with nearly isotropic compressibility, in order to have a better comparison of B_0 values of these two phases, the pressure–volume data are fitted with a second-order Birch–Murnaghan equation of state.[41] The obtained parameters are $B_0 = 100(6)$ GPa for the T-type $In_2Ge_2O_7$ and $B_0 = 170(12)$ GPa for its high-pressure phase. The bulk modulus of the high-pressure phase is much larger as compared to that of the T-type phase. The relatively large difference in bulk moduli appears to be related to the fact that the near neighbor coordination increases at the phase transition.

Table 1 The refined atomic coordinates and lattice parameters for the T-type and P-type $In_2Ge_2O_7$ at ambient pressure and the high-pressure phase of the T-type $In_2Ge_2O_7$ at 17.4 GPa

Compounds	T-type $In_2Ge_2O_7$	P-type $In_2Ge_2O_7$	HP phase (17.4 GPa)
Crystal system	Monoclinic	Cubic	Monoclinic
Space group	$C2/m$ (12)	$Fd\bar{3}m$ (227)	$P2_1/c$ (14)
a/Å	6.6598(3)	9.7121(3)	5.5737(7)
b/Å	8.7842(5)	—	4.0322(6)
c/Å	4.9244(3)	—	4.4102(5)
β/°	102.588(5)	—	105.315(4)
Atoms	Wyckoff (x y z)	Wyckoff (x y z)	Wyckoff (x y z)
In	4g (0 0.3078(4) 0)	16d (0.5 0.5 0.5)	4e (0.2187(2) 0.0315(5) 0.2020(6))
Ge	4i (0.2308(9) 0 0.4079(7))	16c (0 0 0)	4e (0.2187(2) 0.0315(5) 0.2020(6))
O(1)	2c (0 0 0.5)	8b (0.375 0.375 0.375)	4e (0.0705(2) 0.3327(1) 0.3447(4))
O(2)	4i (0.374(4) 0 0.730(6))	48f (0.3244(9) 0.125 0.125)	4e (0.4499(3) 0.7588(9) 0.4793(5))
O(3)	8j (0.2437(6) 0.1685(8) 0.2327(1))	—	—
Residuals[a]/%	R_{wp}: 10.56% R_p: 7.89%	R_{wp}: 6.91% R_p: 6.14%	R_{wp}: 2.34% R_p: 1.86%

[a] R_{wp} and R_p as defined in GSAS.

AC impedance spectra measurement of the T-type $In_2Ge_2O_7$ at high pressures

It has been demonstrated in many cases that the subtle change of structure consequentially brings some influence on the electrical transport properties since the electron transport behavior is closely related to its crystal structure. Therefore, the measurements of AC impedance spectra of the T-type $In_2Ge_2O_7$ are carried out at room temperature. Typical Nyquist plots at different pressures are displayed in Fig. 8. The arc depicts the transportation of charge carrier inside grain. In the pressure range of 0.8–5.3 GPa, with increasing pressures the arc shifts from left to right with increased areas. Above 7.6 GPa, the opposite effect appears. It is worth noting that this area suddenly reduces in the pressure range of 5.3–7.6 GPa. In order to quantify the pressure effect on the electrical transport properties of the T-type $In_2Ge_2O_7$, the impedance spectra are fitted with a commonly equivalent circuit consisting of resistor R and constant phase element (CPE) as shown in Fig. 9 by Zview 2

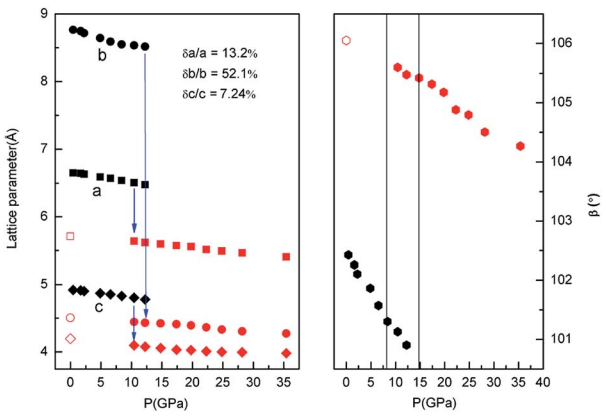

Fig. 5 The lattice parameters as a function of pressure for the T-type $In_2Ge_2O_7$. Closed symbols represent for compression, and open symbols for decompression.

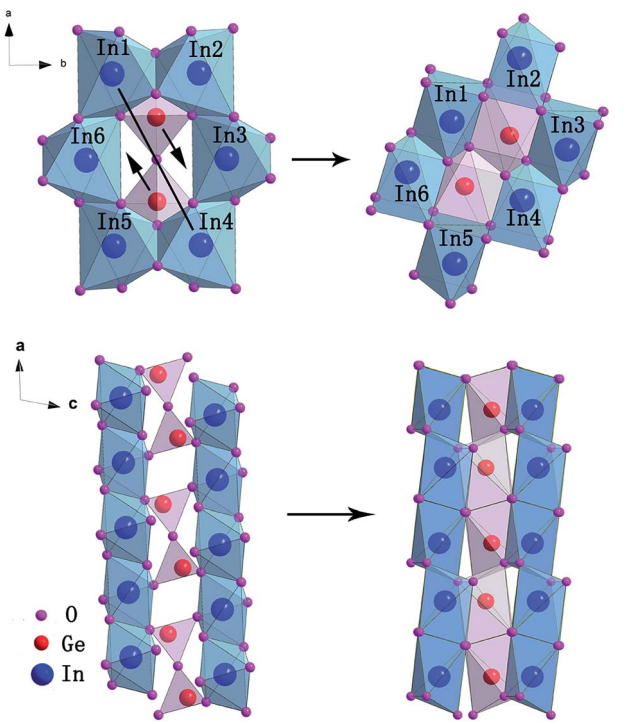

Fig. 6 A schematic representation of the structural transformation of the T-type $In_2Ge_2O_7$ from $C2/m$ to $P2_1/c$ phase in ab and ac plane.

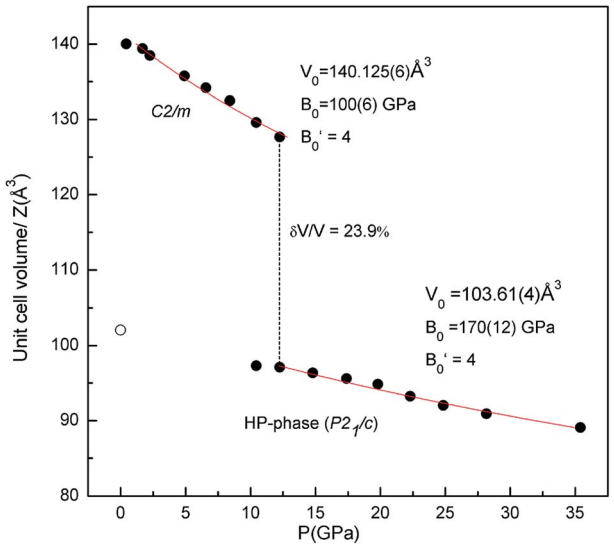

Fig. 7 Observed *P*–*V* variation fitted with the second-order Birch–Murghnan (B–M) equation of state for the T-type $In_2Ge_2O_7$ and its high pressure phase (closed circles for compression and open circles for decompression). The red solid line is the B–M fit of the experimentally observed *P*–*V* data.

impedance analysis software. The value of *R* is directly obtained from the fitting results, as shown in Fig. 10. As can be seen, the resistance of the T-type phase increases with increasing pressure before 5.3 GPa, and after the phase transition, a rapid drop of resistance over two orders of magnitude is observed. With further increasing pressure, the resistance exhibits a smooth decrease for the high-pressure phase. This change of the resistance is consistent with the results of the above XRD data and clearly provides a further proof that the T-type $In_2Ge_2O_7$ undergoes a phase transition under high pressure. Previous study has revealed that the conduction band properties arise primarily from the antibonding B-site ns to O 2p interaction in these compounds.[42] Since the Ge–O–Ge bonds in the T-type $In_2Ge_2O_7$ are highly distorted from nearly linear geometry in its high-pressure phase and the average Ge–O bonding distance decreases upon compression, it can lead to increasing the

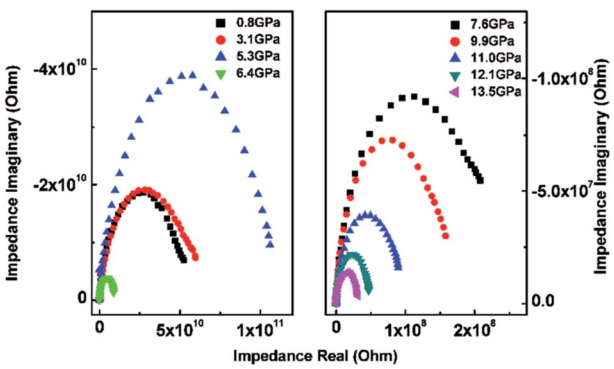

Fig. 8 Nyquist plots of impedance spectra of the T-type $In_2Ge_2O_7$ at high pressures.

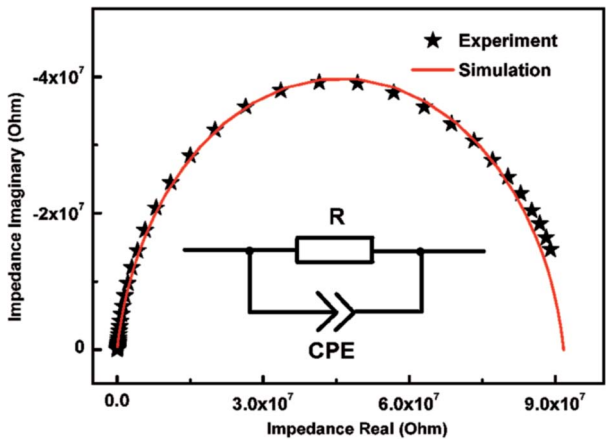

Fig. 9 Equivalent circuit used to represent the electrical properties of grain effects in the T-type $In_2Ge_2O_7$ at 11.0 GPa.

orbital overlap and strengthening the antibonding interaction and thus reducing the resistivity. The T-type phase and new high-pressure phase of $In_2Ge_2O_7$ exhibit different responses to high pressure, which indicates that the excitation across the band gap corresponds to different charge transfer transition in these two phases.

Structural stability of the P-type $In_2Ge_2O_7$ under high pressure

In situ XRD patterns of the P-type $In_2Ge_2O_7$ are collected up to 26.5 GPa at room temperatures and the representative patterns are shown in Fig. 11. There are no splitting or extra peaks appearing in the patterns demonstrating that the cubic phase of the P-type $In_2Ge_2O_7$ remains stable within the whole pressure range. In this ordered pyrochlore structure, all of the atoms are sited on defined positions, except for the O_{48f} atom. Hence, the degree of structural ordering can be determined by the varying of *x* positional parameter of the O_{48f} atom. Previous studies on pyrochlore oxides have revealed that the sudden

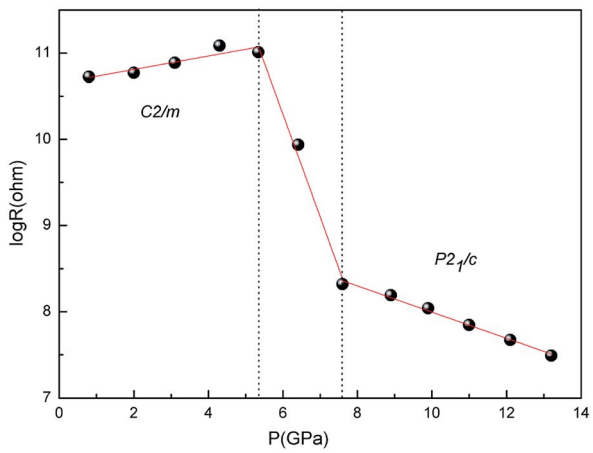

Fig. 10 The resistance of the T-type $In_2Ge_2O_7$ at different pressures. A rapid drop of resistance appeared during the phase transition to its high-pressure phase.

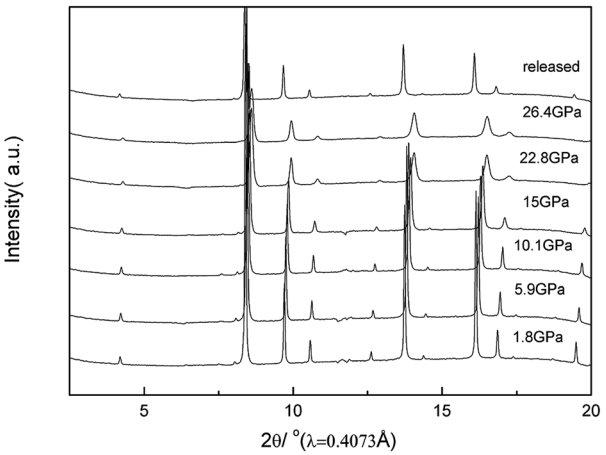

Fig. 11 Selected XRD patterns of the P-type $In_2Ge_2O_7$ with increasing pressure. The pyrochlore structure is stable up to 26.5 GPa.

change of the x positional parameter of the O_{48f} atom existed in the process of pressure-induced structural phase transition. For example, there was a rapid decrease of the x positional parameter with increasing pressure in $Gd_2Zr_2O_7$ implying the phase transition;[35] the x-coordinate of the O_{48f} atom increased dramatically after the transformation in $Sm_2Zr_2O_7$.[34] From our refined results, the x parameter for the O_{48f} atom as a function of pressure does not exhibit any anomaly up to the highest pressure indicating the structural stability in the P-type $In_2Ge_2O_7$, as shown in the inset of Fig. 12.

Pressure dependence of the unit cell volume of the P-type $In_2Ge_2O_7$ is given in Fig. 12. The data are fitted by a second-order Birch–Murnaghan equation of state as the case for the T-type $In_2Ge_2O_7$. The obtained bulk modulus B_0 is 279(4) GPa, quite larger than other ordered pyrochlore oxide materials. For example, the bulk moduli of $A_2Ti_2O_7$ (A = Ho, Y, Tb, Sm) were 213(2), 204(3), 199(1) and 164.8(1.5) GPa, respectively.[43,44] And also for $Gd_2Zr_2O_7$, the bulk modulus was 186(12) GPa.[35]

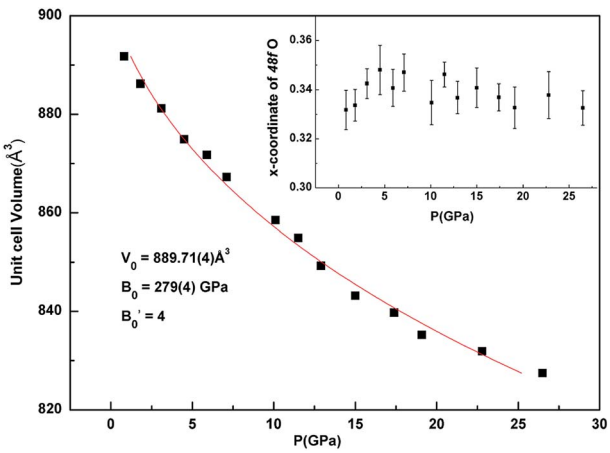

Fig. 12 Observed P–V variation fitted with the second-order Birch–Murghnan (B–M) equation of state for the P-type $In_2Ge_2O_7$. The inset shows the pressure dependence of x parameter for the O_{48f} atom.

Conclusions

The structural stabilities of the monoclinic phase and cubic phase of $In_2Ge_2O_7$ are investigated at high pressures. The T-type $In_2Ge_2O_7$ with the monoclinic ($C2/m$) structure is found to transform to another monoclinic structure ($P2_1/c$) above 6.6 GPa along with a large reduction of atomic volume and an increase of the cation coordination number. The phase transition is sluggish and irreversible. The bulk modulus of the T-type $In_2Ge_2O_7$ is obtained as $B_0 = 100(6)$ GPa, and $B_0 = 170(12)$ GPa is obtained for its high-pressure phase. At the phase transition, an abrupt change is also observed in the electrical transport measurements of the T-type $In_2Ge_2O_7$ above 5.3 GPa, which is correlated to the observed pressure-induced $C2/m$–$P2_1/c$ structural phase transition. However, the P-type $In_2Ge_2O_7$ is much stable up to 26.5 GPa, and the bulk modulus (B_0) is determined to be 279(4) GPa.

Acknowledgements

This work was financially supported by the National Natural Science Foundation of China under Grant no. 51172091, the Program for New Century Excellent Talents in University, China (NCET-12-0240), Jilin Province Science and Technology Development Program, China (20130101023JC). We acknowledge Dr Zhiqiang Chen and Xinguo Hong for technical support with the high-pressure experiments at the X17C beamline of the NSLS synchrotron and thank Dr Yanchun Li at the 4W2 station of the BSRF synchrotron.

References

1 J. Champion, A. Wills, T. Fennell, S. Bramwell, J. Gardner and M. Green, *Phys. Rev. B: Condens. Matter Mater. Phys.*, 2001, **64**, 140407.
2 A. K. Hassan, L. P. Lévy, C. Darie and P. Strobel, *Phys. Rev. B: Condens. Matter Mater. Phys.*, 2003, **67**, 214432.
3 I. Mirebeau, I. N. Goncharenko, P. Cadavez-Peres, S. T. Bramwell, M. J. P. Gingras and J. S. Gardner, *Nature*, 2002, **420**, 54.
4 N. P. Raju, M. Dion, M. J. P. Gingras, T. E. Mason and J. E. Greedan, *Phys. Rev. B: Condens. Matter Mater. Phys.*, 1999, **59**, 14489.
5 A. N. Radhakrishnan, P. Prabhakar Rao, S. K. Mahesh, D. S. Vaisakhan Thampi and P. Koshy, *Inorg. Chem.*, 2012, **51**, 2409.
6 J. Li, T. Siritanon, J. K. Stalick, A. W. Sleight and M. Subramanian, *Inorg. Chem.*, 2011, **50**, 5747.
7 W. J. Weber, N. J. Hess and G. D. Maupin, *Nucl. Instrum. Methods Phys. Res., Sect. B*, 1992, **65**, 102.
8 B. D. Begg, N. J. Hess, D. E. McCready, S. Thevuthasan and W. J. Weber, *J. Nucl. Mater.*, 2001, **289**, 188.
9 W. J. Weber and N. J. Hess, *Nucl. Instrum. Methods Phys. Res., Sect. B*, 1993, **80**, 1245.
10 J. Lian, X. T. Zu, K. V. G. Kutty, J. Chen, L. M. Wang and R. C. Ewing, *Phys. Rev. B: Condens. Matter Mater. Phys.*, 2002, **66**, 054108.

11 S. Lutique, D. Staicu, R. J. M. Konings, V. V. Rondinella, J. Somers and T. Wiss, *J. Nucl. Mater.*, 2003, **319**, 59.
12 M. Hanawa, Y. Muraoka, T. Tayama, T. Sakakibara, J. Yamaura and Z. Hiroi, *Phys. Rev. Lett.*, 2001, **87**, 187001.
13 Y. Machida, S. Nakatsuji, Y. Maeno, T. Tayama, T. Sakakibara and S. Onoda, *Phys. Rev. Lett.*, 2007, **98**, 057203.
14 A. W. Sleight, J. L. Gillson, J. F. Weiher and W. Bindloss, *Solid State Commun.*, 1974, **14**, 357.
15 D. Mandrus, J. R. Thompson, R. Gaal, L. Forro, J. C. Bryan, B. C. Chakoumakos, L. M. Woods, B. C. Sales, R. S. Fishman and V. Keppens, *Phys. Rev. B: Condens. Matter Mater. Phys.*, 2001, **63**, 195104.
16 T. Takeda, M. Nagata, H. Kobayashi, R. Kanno, Y. Kawamoto, M. Takano, T. Kamiyama, F. Izumi and A. W. Sleight, *J. Solid State Chem.*, 1998, **140**, 182.
17 N. Takeshita, C. Terakura, Y. Tokura, A. Yamamoto and H. Takagi, *J. Phys. Soc. Jpn.*, 2007, **76**, 063707.
18 M. J. P. Gingras, C. V. Stager, N. P. Raju, B. D. Gaulin and J. E. Greedan, *Phys. Rev. Lett.*, 1997, **78**, 947.
19 S. T. Bramwell and M. J. Gingras, *Science*, 2001, **294**, 1495.
20 J. S. Gardner, M. J. Gingras and J. E. Greedan, *Rev. Mod. Phys.*, 2010, **82**, 53.
21 J. B. Goodenough and R. N. Castellano, *J. Solid State Chem.*, 1982, **44**, 108.
22 S. J. Korf, H. J. Koopmans, B. C. Lippens, A. J. Burggraaf and P. J. Gellings, *J. Chem. Soc., Faraday Trans. 1*, 1987, **83**, 1485.
23 A. J. Burggraaf, T. van Dijk and M. J. Verkerk, *Solid State Ionics*, 1981, **5**, 519.
24 A. Jaiswal and E. D. Wachsman, *J. Electrochem. Soc.*, 2005, **152**, A787.
25 C. Heremans, B. J. Wuensch, J. K. Stalick and E. Prince, *J. Solid State Chem.*, 1995, **117**, 108.
26 R. Martínez-Coronado, J. Alonso, V. Cascos and M. Fernández-Díaz, *J. Power Sources*, 2014, **247**, 876.
27 D. P. Leusink, F. Coneri, M. Hoek, S. Turner, H. Idrissi, G. Van Tendeloo and H. Hilgenkamp, *APL Mater.*, 2014, **2**, 032101.
28 A. Gutiérrez–Llorente, H. Joress, A. Woll, M. E. Holtz, M. J. Ward, M. C. Sullivan, D. A. Muller and J. D. Brock, *APL Mater.*, 2015, **3**, 036105.
29 L. Bovo, X. Moya, D. Prabhakaran, Y.-A. Soh, A. T. Boothroyd, N. D. Mathur, G. Aeppli and S. T. Bramwell, *Nat. Commun.*, 2014, **5**, 3439.
30 W. Tian, C. Zhi, T. Zhai, X. Wang, M. Liao, S. Li, S. Chen, D. Golberga and Y. Bandoa, *Nanoscale*, 2012, **4**, 6318.
31 R. D. Shannon and A. W. Sleight, *Inorg. Chem.*, 1968, **7**, 1649.
32 A. F. Reid, C. Li and A. E. Ringwood, *J. Solid State Chem.*, 1977, **20**, 219.
33 M. A. Subramanian, *Mater. Res. Bull.*, 1992, **27**, 939.
34 F. X. Zhang, J. Lian, U. Becker, L. W. Wang, J. Hu, S. K. Saxena and R. C. Ewing, *Chem. Phys. Lett.*, 2007, **441**, 216.
35 F. X. Zhang, J. Lian, U. Becker, R. C. Ewing, J. Hu and S. K. Saxena, *Phys. Rev. B: Condens. Matter Mater. Phys.*, 2007, **76**, 214104.
36 F. X. Zhang, B. Manoun and S. K. Saxena, *Mater. Lett.*, 2006, **60**, 2773.
37 Y. Su, S. Li, L. Xu, Y. Chen, Q. Zhou, B. Peng, S. Yin, X. Meng, X. Liang and Y. Feng, *Nanotechnology*, 2006, **17**, 6007.
38 L. Li, P. S. Lee, C. Yan, T. Zhai, X. Fang, M. Liao, Y. Koide, Y. Bando and D. Golberg, *Adv. Mater.*, 2010, **22**, 5145.
39 H. K. Mao, J.-A. Xu and P. M. Bell, *J. Geophys. Res.*, 1986, **91**, 4673.
40 A. C. Larson and R. B. Von Dreele, GSAS, LANSCE, MS -H805, Los Alamos National Laboratory, Los Alamos, NM 87545, LAUR 86–748, Vers. 2000.
41 F. Birch, *J. Geophys. Res.*, 1978, **83**, 1257.
42 H. Mizoguchi, H. W. Eng and P. M. Woodward, *Inorg. Chem.*, 2004, **43**, 1667.
43 P. R. Scott, A. Midgley, O. Musaev, D. Muthu, S. Singh, R. Suryanarayanan, A. Revcolevschi, A. Sood and M. Kruger, *High Pres. Res.*, 2011, **31**, 219.
44 F. X. Zhang, B. Manoun, S. K. Saxena and C. S. Zha, *Appl. Phys. Lett.*, 2005, **86**, 181906.